UC Davis
UC Davis Previously Published Works

Title

A nephrotoxicity-free, iron-based contrast agent for magnetic resonance imaging of tumors

Permalink

Authors

Xue, Xiangdong
Bo, Ruonan
Qu, Haijing
et al.

Publication Date

2020-10-01

DOI

10.1016/j.biomaterials.2020.120234

Peer reviewed

A Nephrotoxicity-free, Iron-Based Contrast Agent for Magnetic Resonance Imaging of Tumors

Xiangdong Xue[1], **Ruonan Bo**[1,2], **Haijing Qu**[1], **Bei Jia**[1], **Wenwu Xiao**[1], **Ye Yuan**[1], **Natalia Vapniarsky**[3], **Aaron Lindstrom**[1], **Hao Wu**[1], **Dalin Zhang**[1], **Longmeng Li**[1], **Marina Racci**[1], **Zhao Ma**[1], **Zheng Zhu**[4], **Tzu-yin Lin**[4], **Angelique Louie**[5], **Yuanpei Li**[1]

[1]Department of Biochemistry and Molecular Medicine, UC Davis Comprehensive Cancer Center, University of California Davis, Sacramento, California, 95817, USA.

[2]School of Veterinary Medicine, Yangzhou University, Yangzhou 225009, PR China.

[3]Department of Pathology, Microbiology, and Immunology, University of California, Davis, Davis, CA 95616, USA.

[4]Division of Hematology and Oncology, Department of Internal Medicine, School of Medicine, University of California Davis, Sacramento, CA 95817, USA.

[5]Department of Biomedical Engineering, University of California Davis, Davis, California, 95616, USA.

Abstract

Gadolinium-based contrast agents (GBCAs) are the most widely used T_1 contrast agents for magnetic resonance imaging (MRI) and have achieved remarkable success in clinical cancer diagnosis. However, GBCAs could cause severe nephrogenic systemic fibrosis to patients with renal insufficiency. Nevertheless, GBCAs are quickly excreted from the kidneys, which shortens their imaging window and prevents long-term monitoring of the disease per injection. Herein, a nephrotoxicity-free T_1 MRI contrast agent is developed by coordinating ferric iron into a telodendritic, micellar nanostructure. This new nano-enabled, iron-based contrast agent (nIBCA) not only can reduce the renal accumulation and relieve the kidney burden, but also exhibit a

significantly higher tumor to noise ratio (TNR) for cancer diagnosis. In comparison with Magnevist (a clinical-used GBCA), Magnevist induces obvious nephrotoxicity while nIBCA does not, indicating that such a novel contrast agent may be applicable to renally compromised patients requiring a contrast-enhanced MRI. The nIBCA could precisely image subcutaneous brain tumors in a mouse model and the effective imaging window lasted for at least 24 h. The nIBCA also precisely highlights the intracranial brain tumor with high TNR. The nIBCA presents a potential alternative to GBCAs as it has superior biocompatibility, high TNR and effective imaging window.

Keywords

nanoparticle; contrast agents; magnetic resonance imaging; tumor imaging; nephrotoxicity-free

1. Introduction

The continuous decline in cancer mortality over the past three decades can be attributed to the emergence of more sophisticated diagnostic techniques and improved therapeutic approaches. If the tumor can be diagnosed at an early stage and treated in a timely manner, the cure rate could be improved due to the prevention of metastasis and drug resistance development.[1] MRI exhibits a myriad of merits and has been widely utilized in cancer diagnosis to provide exquisite details of the lesion with anatomical and functional information. However, MRI is not as sensitive as nuclear medicine imaging[2–5] and optical imaging[6–8], especially when the contrast between the lesion and the normal tissue is marginal. To improve the contrast, exogenous contrast agents (CAs)[9, 10] are generally administered to patients prior to MRI. CAs are employed to shorten the longitudinal (T_1) or transverse (T_2) relaxation time of the adjacent water protons and lead to higher MR signals as a function of CA accumulation in tissues, thus improving the imaging sensitivity. In clinical practice, T_1 CAs are more desirable than T_2 CAs in tumor diagnosis because T_2 MRI exhibits dark signals which can be confused with signal dropout generated by bleeding or calcification.[11, 12] While superparamagnetic iron oxide nanoparticles (SPIONs) are the most commonly used T_2 CAs, they are susceptible to a "blooming effect" caused by the mutual interference between the CAs and a local magnetic field.[13] T_1 MRI enhancements are mostly performed with the infusion of gadolinium-based contrast agents (GBCAs)[14, 15] which have been administered clinically more than 100 million times and have achieved remarkable success in the clinic.[16, 17] However, safety issues with GBCAs emerged a decade ago and a wealth of evidence showed that linear GBCAs were associated with nephrogenic system fibrosis (NSF). This serious condition is most commonly the result of high dose, and/or repeated administrations of linear chelation-based GBCAs in patients with renal insufficiency.[18–20] More recently, GBCAs have been associated with long-term gadolinium retention in central nervous system.[20, 21] These safety concerns have led to the restriction of linear GBCAs by the European Medicines Agency (EMA) and a "black-box warning" on GBCAs by the FDA.[22, 23]

Due to these concerns associated with the use of GBCAs, scientists are seeking safer alternatives. Researchers tried to stabilize the gadolinium coordination in the CAs to minimize the demetallation and reduce their toxicity if the GBCAs accumulate in kidney.

[24] However, heavy metals like gadolinium cannot be metabolized and CAs using it may still induce toxicity eventually if the CAs are retained in sufficient concentration. Most often, GBCAs tend to be excreted from the kidney because of their susceptibility to glomerulus filtration.[25, 26] Their quick kidney elimination may be beneficial in certain clinical settings for quick diagnosis but on the other hand may shorten the imaging window of using GBCA-mediated MRI for tracking dynamic changes in the long-term in the body. Since nanoparticles of a certain size are not easily excreted by the kidneys, manganese oxide nanoparticles (MnO NPs) have been developed[27–29] for T_1 MRI and are potential GBCAs alternatives. However, inorganic MnO NPs are not readily metabolized, which may cause them to accumulate in other organs and induce neurodegenerative disorder known as manganism. Another alternative is iron, as it is ubiquitous in organisms and more biocompatible than gadolinium- or manganese-based CAs because iron ions generally have a high toxicity threshold and are often used as non-toxic supplements. More importantly, several iron oxide nanoparticles have been approved for human use by the FDA. For instance, Ferumoxytol is used as an iron supplement, while Ferucarbotran and Ferumoxide are approved for the reticuloendothelial system (RES) T_2 MRI. For safety considerations, iron-based CAs are ideal alternatives to GBCAs on MRI. As a paramagnetic metal ion, ferric iron has 5 unpaired electrons and exhibits a high longitudinal relaxivity (r_1) for T_1 MRI. However, most commonly used iron-containing nanoparticles, like SPIONs, have mainly been investigated for T_2 MRI applications[30–32], as the strong transversal relaxivity (r_2) derived from the high magnetic moments of SPIONs themselves hinder iron from being used as T_1 MRI. Interestingly though, when SPIONs are made in an ultra-small size (usually less than 4 nm), the T_1 effect becomes dominant.[33–35] Unfortunately, nanoparticles with a size less than 5 nm are easily excreted through the kidneys,[36] which gives ultra-small SPION undesirable pharmacokinetics. Ferric iron and organic molecules coordinated complexes exhibited excellent T_1 MRI signals. Davies and co-workers developed an iron-organic molecule coordinate for T_1 MRI, but this CA still showed a short imaging window and had obvious accumulation in the kidneys[37]. Ling and coworkers developed a CAs that contained ferric iron by coordination with catechols.[38] The iron-containing CAs showed competitive relaxivity to GBCAs, but the effective imaging window only lasted for 2.5 h. Iron-based, nanoscale T_1 CAs were also developed by Gianneschi's group[39] and Chalermchai's group[40], which both showed high relaxivity. However, they have not yet applied their materials to *in vivo* imaging. Thus, there is still a need for new designs in nontoxic, long-circulating T1 contrast agents.

To identify a tumor, the ratio between tumor tissue and normal tissue (TNR) should be as high as possible, so that tumors can be readily differentiated from the normal tissues.[41] MRI CAs should be able to selectively accumulate in the tumor tissue, which enhances the MRI signal only in tumors and generates a high TNR. Small molecule CAs, like GBCAs, are not only susceptible to premature clearance during systemic circulation, but also lack the tumor selectivity for tumor tissues. This lack of sensitivity results in a high background signal from normal tissue that may confound the imaging readouts. Nanoparticles can selectively accumulate in solid tumor tissue either by the enhanced permeability and retention (EPR) effect[42–44] or transcytosis[45], which could improve the sensitivity, accuracy and TNR of MRI-based tumor diagnosis agents. Nanoparticle-based CAs maintain

a relatively long retention time within tumors and have longer effective imaging windows for the diagnosis,[46, 47] which is beneficial to long-term imaging and computational reconstruction.[48, 49]

Development of T_1 MRI CAs with less toxicity and high tumor selectivity is urgently required for sensitive imaging and tumor diagnosis. To this end, iron-based, nanoscale CAs are ideal candidates for T_1 MRI because of the following advantages i) iron has lower systemic toxicity in comparison to gadolinium; ii) the nanoscale structure tends to accumulate in the tumor site, thus contributes higher TNR; iii) the nanostructure bypasses the quick kidney excretion to show both low nephrotoxicity and a long imaging window. Our group has developed telodendrimer-based micellar nanoparticles which have shown remarkable tumor selectivity and long-term tumor retention.[47, 50–52] Inspired by the telodendrimer, we developed a novel nano-enabled, iron-based contrast agent (nIBCA) with significantly improved TNR for MRI, impressively reduced kidney accumulation, and lowered kidney burdens (Scheme 1). The building blocks of nIBCA are novel telodendritic molecules composed of a hydrophilic PEG tail and a hydrophobic iron-based dendritic oligomer. The PEG tail is attached to the dendritic oligomer by iron coordination with the catechol functional groups on nordihydroguaiaretic acid (NDGA) to form a telodendritic structure. Unlike our previous telodendrimers that require tedious multiple-step synthesis, this new building block can be synthesized *via* one-step coordination chemistry. This amphiphilic, telodendritic structure can readily self-assemble into a micellar nanostructure (nIBCA), in which the iron coordination endows the nIBCA with enhanced T_1 MRI capabilities. The nIBCA selectively accumulates at the tumor site and enables enhanced imaging of the tumor site with a strong T_1 MRI signal and improved TNR. In comparison with Magnevist (a clinical-used GBCA), Magnevist shows poor tumor selectivity, which not only accumulates in tumor site, but also distributes in normal tissues, and thereby, leads to lower TNR to nIBCA. Moreover, the nIBCA shows imperceptible nephrotoxicity in a well-established kidney disease mouse model because the nanoparticle is not susceptible to kidney excretion. In contrast, Magnevist can easily diffuse into the kidney to incur potential nephrotoxicity. The nIBCA is also able to indicate both subcutaneous and intracranial brain tumors in mouse models.

2.   Materials and Methods

2.1.   Materials and Instruments.

Unless otherwise stated, all reagents were purchased from commercial suppliers and used without further purification. The chemical structure of iron-based telodendrimer was characterized by matrix-assisted laser desorption/ionization-time of flight mass spectrometry (MALDI-TOF MS, UltraFlextreme, Bruker, German), nuclear magnetic resonance (NMR, 600 MHz, Bruker, German) and inductively coupled plasma mass spectrometry (ICP-MS, Agilent Technologies, 7500ce). The morphology of the nanoparticles was observed by transmission electron microscopy (TEM, Talos L120C, FEI, USA) with 80 kV acceleration voltage. Size distribution and surface charge of the nanoparticles were evaluated by dynamic light scattering (DLS, Nano-ZS, Malvern, UK). UV-vis absorbance was obtained by a UV-vis spectrometer (UV-1800, Shimadzu, Japan). All MRI experiments were conducted on a

Biospec 7T MRI (Bruker, German). The biodistribution of iron was quantitively analyzed by an inductively coupled plasma mass spectrometry (ICP-MS, Agilent Technologies, 7500ce).

2.2. Synthesis and purification of PEG-catechol.

273 mg 3,4-Dihydroxyhydrocinnamic acid (1.5 mmol), 576 mg EDC and 690 mg NHS were dissolved in DMF and vigorously stirred for 30 min. Then, 1.1 g mPEG$_{2000}$-NH$_2$ were added into the reaction system. 24 h later, the reaction system was precipitated by cold ether (−20 °C) for 5 times. The precipitation was further dialyzed in a dialysis tube (MWCO=1 kDa) overnight. The solution in the tube was lyophilized, yielded white product.

2.3. Synthesis and purification of iron-coordinated telodendrimer.

237 mg PEG-catechol (0.1 mmol), 604 mg nordihydroguaiaretic acid (NDGA, 2 mmol) and 540 mg FeCl$_3$·6H$_2$O (2 mmol) were dissolved in anhydrous methanol and refluxed overnight. The reaction system was precipitated with cold ether for 5 times to get the compounds which contained PEG. Then, the precipitation was dialyzed in a dialysis tube (MWCO=1 kDa) to eliminate NDGA and FeCl$_3$·6H$_2$O. The compounds remained in the dialysis tube were lyophilized and deep brown flakes were yielded. To remove the extra PEG-catechol and iron coordinated PEG-PEG compounds, we assembled the brown flakes in water by a reprecipitation method. Briefly, the flakes were dissolved in tetrahydrofuran, then dropped into water under vigorous stirring, the nanoparticles were formed once the tetrahydrofuran completely evaporated. The raw nanoparticles were purified by centrifugal dialysis (MWCO=30 kDa). Since PEG-catechol and iron coordinated PEG-PEG compounds cannot form nanoparticles, they were removed in this step. The compound that remains in the centrifugal dialysis tube was lyophilized to yield the final iron-coordinated telodendrimer.

2.4. Preparation of nano-enabled, iron-based contrast agent (nIBCA).

The nIBCA was prepared by a nanoprecipitation method.[53–55] In brief, 10 mg iron-coordinated telodendrimer was dissolved in 300 μL tetrahydrofuran, and the solution was then dropped into 1 mL water under vigorous stirring. The mixed solution was stirred under ambient temperature. The nIBCA was obtained after tetrahydrofuran was completely evaporated. The nIBCA can be well-suspended in water with a high concentration about 500 mg/mL.

2.5. UV-vis absorption measurements.

The UV-vis absorption of water solution of 5 μM of iron-coordinated telodendrimer, and its corresponding concentrations of PEG-catechol, FeCl$_3$·6H$_2$O and NDGA were recorded by a UV-vis spectrometer (UV-1800, Shimadzu). The recorded range was set from 500 to 250 nm. The quartz cuvette was with a path length of 1 mm.

2.6. Stability of nIBCA.

10 mg/mL nIBCA were incubated with 10% fetal bovine serum (FBS) at room temperature. The hydrodynamic size and polydispersity index (PDI) of nIBCA was monitored by DLS.

2.7. Hemolysis evaluation.

Fresh citrated blood was obtained from healthy human volunteers. The blood was diluted with PBS for 6 times and centrifuged (1000 g for 10 min) to separate the red blood cells (RBCs). The RBCs were washed with PBS for three times and resuspended in PBS for further use. 200 μL diluted RBC suspension was mixed with nIBCA in different final concentrations (1, 10, 100, 1000 μg/mL) by gentle vortex. The mixture was incubated at 37 °C for 4 h. Then, the mixtures were centrifuged (1000 g for 5 min), and the supernatants were transferred to 96-well plate for UV-vis absorbance measurement. The absorbance at 540 nm was collected to determine the hemolysis of the samples. RBCs incubation with Triton-100 (2%) and PBS were used as the positive and negative controls, respectively. The percentage of the hemolysis was calculated by a formula: RBCs hemolysis = (OD_{sample} − $OD_{negative\ control}$)/($OD_{positive\ control}$ − $OD_{negative\ control}$) × 100%.

2.7. Cell viability of nIBCA in different brain tumor cell lines.

U-251 MG glioblastoma cells, glioma 261 cells (GL261), human brain glioma cells (U-118 MG Line), human U87 glioblastoma cells were seeded in 96-well with a cell density of 5,000 per well, respectively. The cells were incubated for 24 h until fully attached. Then, the cell culture medium of these cells was replaced with medium containing different concentrations of nIBCA. The cells were incubated with nIBCA for 24 h and subjected to standard MTT assay. Each treatment was set as triplicates.

2.8. Evaluation of critical micelle concentration (CMC)

Pyrene was employed as an indicator of the CMC evaluation.[56, 57] In brief, nIBCA was diluted into different concentrations, including 0.0512, 0.256, 1.28, 6.4, 32, 160, 800, 4000 μg/mL, and incubated with 0.2 μM pyrene for 2 h at ambient temperature. The fluorescence spectra of pyrene in the nIBCA dilutions were measured. The fluorescence intensities at 375 nm and 391 nm were compared for CMC calculation.

2.9. MRI of nIBCA in subcutaneous and orthotopic brain tumor models.

100 mg/kg of nIBCA or 67 mg/kg of Magnevist were i.v. administrated into brain tumor-bearing mice (n=3). 100 mg/kg nIBCA and 67 mg/kg Magnevist contained the same amounts of the metal (iron in nIBCA and Gd in Magnevist). The mice were then anesthetized and transported to the imaging chamber for MRI. All MRI experiments were conducted with a Bruker Biospec 7 T MRI scanner using the T_1-weighted Multi-Slice Multi Echo (MSME) sequence with echo time (TE) of 14 ms and repetition time (TR) of 300 ms. The matrix size is 256×256, and the field of view (FOV) is 8 cm*8 cm.

2.10. Establishment of the kidney disease model.

To establish the kidney disease (KD) model, the C57BL/6 mice were i.p. injected cisplatin (7.5 mg/kg) for three consecutive weeks (once per week). After three doses of treatment, the blood and kidney of the mice were collected for hematological and histopathological analysis which could confirm the kidney conditions. To prove the nephrotoxicity of nIBCA and Magnevist, we designed 4 groups of treatment (n=3): i) Negative control. Mice were raised as normal, without giving any treatment; ii) mice with KD; iii) KD mice treated with

nIBCA; iv) KD mice treated with Magnevist. The KD mice were treated with three doses (once per day) of nIBCA (100 mg/kg) or Magnevist (67 mg/kg). After three doses of treatment, the mice were sacrificed for hematological and histopathological analysis. All animal experiments were strictly in compliance with the guidelines of Animal Use and Care Administrative Advisory Committee (IACUC) of the University of California, Davis.

2.11. Pharmacokinetic evaluation

100 mg/kg nIBCA and 67 mg/kg Magnevist were i.v. administrated into nude mice (n=3). Then, 10 μL fresh blood was collected through tail vein at different time points (2, 5, 10, 15, 20, 25, 30, 40, 50, 60, 90, 120, 150, 180, 240, 360, 480, 1440, 2880, 4320 min). The blood was dissolved in 990 μL DMSO right after the collection. Then, the DMSO solution was applied to ICP-MS analysis. The concentrations of iron and gadolinium were quantified for the pharmacokinetics of nIBCA and Magnevist respectively. Blood collected before the administration of the material was set as background to deduct the endogenic iron and gadolinium contents.

2.12. Biodistribution of nIBCA.

The mouse tissues (50~200 mg) from heart, liver, spleen, lung, kidney and tumor were transferred into clean plastic microcentrifuge tubes. 2 mL of concentrated nitric acid was added until the tissues were completely soaked. The tissues and nitric acid were incubated at ambient temperature overnight in a fume hood. Then, the tubes were placed on a hot plate (90 °C) to digest the tissues until the volume reduces to ~400 μL. The digested tissues were transferred and diluted with Milli-Q water for 10 times in a clean tube. The final concentration of nitric acid was diluted to 2% to water (vol/vol). Then, the digested tissues were placed in room temperature for iron and gadolinium quantification by ICP-MS analysis.

2.13. Subcutaneous and intracranial brain tumor model establishment.

For subcutaneous tumor models, 1×10^6 U251-MG cells were inoculated onto the right flank of the nude mice (female, 4-week old), the subcutaneous tumors were developed in around 4 weeks. For the intracranial brain tumor model, a tiny hole was drilled on the skull of the mouse with a small animal stereotaxic instrument. 5×10^4 U251-MG cells were then carefully inoculated into the brain of the nude mice (female, 4-week old) with a microliter syringe. Then, the skin on the head was sutured. The mice were given analgesics to relieve the pain. After 2~3 weeks of good care, the orthotopic brain tumors were developed.

2.14. Tumor selectivity of nIBCA

A hydrophobic dye (DiD) was encapsulated into nIBCA to form a fluorescently traceable nanoparticle (nIBCA@DiD). 100 mg/kg nIBCA@DiD was i.v. administrated into mice with an orthotopic brain tumor. In 24 h, the whole brain of the nIBCA@DiD treated mice was harvest and cryo-sliced for CLSM observation. The whole-brain slices were also stained with Hoechst 33342 to indicate the nuclei. DAPI channel was used for observing the nuclei and DiD standard channel was for tracking the nIBCA. The adjacent brain slices were also stained by H&E to locate the tumor and normal tissues in the brain.

2.15. H&E and hematology evaluation.

100 mg/kg nIBCA was i.v. administrated into subcutaneous brain tumor-bearing mice for tumor MRI. After 48 h imaging, blood of these mice was collected for hematology analysis; the major organs were sliced and stained with hematoxylin and eosin (H&E) to evaluate the toxicity. The main organs include heart, liver, spleen, lung and kidney. The PBS-treated mice were employed as control.

2.16. Statistics analysis.

The statistical analysis was conducted by *t-test* between two groups, and One-way ANOVA analysis of variations for multiple groups. All results were expressed as the mean $\pm$ s.d. A value of $p < 0.05$ was considered statistically significant.

3. Results and Discussion

3.1. Synthesis and characterization of iron-based telodendrimer.

To build nIBCA, the linear hydrophilic tail was first synthesized. PEG_{2000}-amine was conjugated with 3,4-dihydroxyhydrocinnamic acid (DHCA) through an amide bond to introduce a catechol moiety to the PEG chain (Figure S1). The mass spectra (Figure S2) and nuclear magnetic resonance (NMR) spectrum (Figure S3) both indicated that the PEG-catechol was successfully synthesized. Catechol ligands show high affinity to ferric iron and have been widely utilized to develop iron-catechol coordinated materials.[58–60] Inspired by these materials, we dissolved $FeCl_3$, NDGA (with two catechols in the structure) and PEG-catechol in methanol, the mixture was refluxed overnight to form the iron-coordinated telodendrimer (ICT, Figure S4). As illustrated in Figure S5, the reaction system was initially precipitated with cold ether to remove the leftover reactants that lack PEG (e.g. NDGA, $FeCl_3$ and iron-NDGA complex), then dialyzed with dialysis tubing (MWCO=1 kDa) for further purification. We assembled the crude product into nanoparticles because PEG-catechol molecules cannot be removed by ether precipitation and dialysis. Since PEG-catechols are not able to assemble into nanoparticles (Figure S6), we employed centrifugal dialysis (MWCO=30 kDa) to get rid of the unreacted PEG-catechols or residual PEG-iron complexes. In this case, nanoparticles cannot pass through centrifugal dialysis (Figure S7) and the final compounds that retained in the dialysis tube should be the amphiphilic ICT. As the presence of ferric iron strongly interfered the NMR analysis, we employed alternative methods to confirm the chemical structure of the final product. First, ICP-MS was employed to quantify the percentage of the iron in the proposed ICT. As shown in Table S1, 1031 ng of iron were detected in 0.025 mg of ICT, indicating that ferric iron accounted for 4.124% of the whole molecules. The final product was also analyzed by mass spectrometry (Figure S8) and the mass spectrum showed a cluster of mass peaks which were attributed to be a normal distribution of PEG molecules. The average molecular weight was around 4,200 Da. Besides one molecule of PEG-catechol (2,200 Da), the rest of the molecular weight can be assigned to 6 molecules of NDGA (~1812 Da) and 3 molecules of iron (~168 Da), with that overall mass coming very close to 4,200 Da. In this case, the percentage of iron in the whole complex was around 4% (168/4200), which closely fit the ICP-MS quantification results. Based on these results, the chemical structures of the telodendrimer were proposed in Figure S9. There are two possibilities for the telodendrimer structures with two different branches

lengths on the dendrimer side based on these results. The evenly distributed branches (left) should be dominant as the steric hindrance of uneven branches (right) would be significantly higher.

3.2. Characterization of iron-based contrast agent.

After the structures were defined, the ICTs were self-assembled into nano-enabled iron-based CAs (nIBCA, Figure S10) by the nanoprecipitation method[53–55] and their size distribution was tested by dynamic light scattering. As shown in Figure 1a, the hydrodynamic diameter was 66 nm, with a polydispersity index of 0.161, indicating that nIBCA is quite homogeneous. The surface charge of nIBCA is −10.5 mV (Figure S11). This negatively charged PEG surface may be beneficial to slow down the elimination of CA by opsonization and contribute to the tumor accumulations of nIBCA.[61, 62] The morphology of the nIBCA was observed by TEM. As shown in Figure 1b, nIBCA exhibited micellar structures with spherical morphology. It is worth noting that the micellar structure can be readily observed without the negative stain that is usually needed to observe soft materials with TEM. The micellar structure was clearly sketched by a high contrast rim, indicating that iron was evenly distributed along with the spherical nanostructure. The DLS and TEM results demonstrated that the nIBCA was successfully constructed. The stability of nIBCA was tested in the presence of serum and the nIBCA remained stable in size and PDI for more than a week (Figure 1c). The critical micellar concentration of nIBCA was 7.12 μg/mL, and it increased slightly to 8.35 μg/mL in 9 days (Figure S12). Such minor changes in CMC further demonstrated that nIBCA was with good stability. The UV absorbance of the individual reactants (PEG-catechol, NDGA and $FeCl_3$, respectively), a physical mixture of the reactants, and ICT were evaluated (Figure 1d). For the individual reactants, PEG-catechol and NDGA both exhibited a characteristic peak around 280 nm due to the presence of their aromatic rings, while $FeCl_3$ showed whole-spectral absorbance without any characteristic peak. By physically mixing the reactants together, the overall absorbance at 280 nm was elevated, which was ascribed to the superposition of the absorbance of PEG-catechol and NDGA, while the spectrum of $FeCl_3$ was suppressed by strong absorbance of the aromatic rings. The UV absorbance of ICT showed full-spectrum absorption with a tiny red-shifted peak in the area of the aromatic rings. The difference between ICT and the mixture supported the idea that iron coordination had occurred in the ICT complexes. As an MRI probe, the relaxivity (r_1) of nIBCA was measured to be 3.951 mM^{-1} S^{-1} (Figure 1e) which was close to the r_1 of Magnevist (r_1=4.565 mM^{-1} S^{-1}, Figure S13). Collectively, the nIBCA had a stable micellar structure with a negatively charged PEG surface and a relaxivity close to Magnevist, which suggested that it would be effective as a tumor MRI agent in animal models. Before being applied to animal models, the blood compatibility of the nIBCA was investigated and as shown in Figure 1f and Figure S14, nIBCA didn't cause obvious hemolysis.

3.3. Cell viability of nIBCA in different brain cell lines.

Prior to the animal applications, the biocompatibility of nIBCA was evaluated at the cellular level by evaluation of the cell viability. We employed nIBCA to treat 4 different brain tumor cells, including U-251 MG glioblastoma cells, glioma 261 cells (GL261), human brain glioma cells (U-118 MG Line), human U87 glioblastoma cells, and applied to MTT assay.

As shown in Figure S15, the nIBCA exhibited imperceptible toxicity to these cells, indicating that our nano-enabled contrast agent was with good bio-safety.

3.4. Application of nIBCA to subcutaneous brain tumor model.

To investigate the MRI capabilities of nIBCA, we applied it to a subcutaneous mouse model established with U-251 MG glioblastoma cells. A representative GBCA, Magnevist, was employed as a control. The nIBCA was intravenously (i.v.) administrated into tumor-bearing mice and the tumors were monitored by T_1-weighted MRI at different time points. As shown in Figure 2a, the MRI signal at the tumor site was gradually enhanced by nIBCA in a time-dependent manner (upper panel). With time elapse, the MRI signal increased to a peak signal at 24 h, then decreased at 48 h after the administration of nIBCA (Figure 2a and 2b). The decrease of TNR from 24 h to 48 h can be attributed to the metabolic clearance of the nIBCA, which led to weaker MR signal at tumor site. The nIBCA could selectively accumulate at the tumor site and reduce its non-specific distribution in normal tissues. Therefore, nIBCA should have an enhanced MRI signal within the tumor and has very little background signal from the normal tissue. As shown in Figure 2c, the MR signal of the tumor was at the same level as the normal tissue (TNR was around 1) before nIBCA administration. The TNR gradually increased with the accumulation of nIBCA, the signal in tumor region was about 2 times higher than the normal tissue. The high TNR demonstrated that nIBCA had superior tumor imaging capabilities and could selectively enhance the contrast of tumor with minimal signal interferences from normal tissues. To monitor whether nIBCA increased the kidney burden, the kidney accumulation of nIBCA was also monitored by MRI. nIBCA didn't exhibit any obvious kidney accumulation (lower panel of Figure 2a and Figure 2d), as no significant MR signal increased in the kidneys after the nIBCA administration, indicating that nIBCA may induce less nephrotoxicity in patients with kidney disease. In striking contrast, Magnevist enhanced the MR signal within a short time (Figure S16a, S16b). The tumor was visualized at 10 min and the signal tapered off in 90 min. Meanwhile, the normal tissues also showed strong T_1 MRI signal and Magnevist exhibited low TNR (Figure S16c). Only the images at 10 min showed a significant difference in comparison with that at 0 min, indicating that Magnevist not only enhanced the T_1 contrast in the tumor, but also non-specifically enhanced the signal in normal tissues. As expected, the small-molecule GBCA showed an overwhelmingly strong signal in the kidneys (lower panel of Figure S16a, S16d). The MRI signal in the kidneys at 30 min was ~4 times higher than the MRI signal at 0 min and stayed at a high level for more than 90 min. Overall, these results indicate that Magnevist has a considerable accumulation in the kidneys, which may be the reason why GBCA is potentially fatal to patients with kidney insufficiency. When comparing the TNRs between nIBCA and Magnevist at their maximum T_1 MRI signal, the nIBCA-mediated MRI exhibited a significantly higher TNR than Magnevist did (Figure 2e). In addition, the MRI imaging window of nIBCA, at least 24 h, was much longer than that of Magnevist, around 1~1.5 h. The fast signal drop in the Magnevist signal was attributed to its quick removal from the blood by the kidneys, which can be confirmed by the MRI of the kidneys (Figure S16a, lower panel). The 24-time longer imaging window of nIBCA is beneficial to long-term monitoring of the tumor or for tumor reconstructions that may provide more detailed information.

3.5. Evaluation of nephrotoxicity of nIBCA and Magnevist.

Next, the nephrotoxicity of nIBCA was investigated using a mouse model of kidney disease (KD) and Magnevist was employed as a control. To establish the KD model, C57BL/6 strain mice (n=3) were intraperitoneally (i.p.) injected with 7.5 mg/kg cisplatin once per week for three consecutive weeks (Figure 3a). Cisplatin is known to be cleared by glomerular filtration and tubular secretion which leads to its accumulation in the renal tubules, thus causes direct toxicity to the kidneys.[63, 64] As shown in Figure 3b, the kidney morphology of the cisplatin-treated mice changed and obvious cortical tubular epithelial damage can be found in the proximal convoluted tubules. Histopathological changes were manifested by cellular ballooning degeneration, sloughing into the tubular lumen, and individual cell necrosis with nuclear shrinkage and fragmentation. Multiple (approximately 60%) tubules were lined by attenuated epithelium (regeneration). The necrotic cells occasionally occluded luminal space and formed cellular casts. Glomeruli were not affected, but an occasional thickening of the basement membrane was observed. In the hematological analysis, we observed that the infusion of cisplatin decreased the glomerular filtration rate (GFR) of the kidney, which resulted in a significant elevation of creatinine and blood urea nitrogen (BUN) levels (Figure 3c and 3d). This evidence all supported the conclusion that the physiological condition of the kidney was altered and that the KD mouse model was successfully established. The KD mouse models (cisplatin-treated mice) were then treated with Magnevist and nIBCA, respectively. The mice received three doses of the contrast agents by i.v. injection (one dose per day). The mice were sacrificed thereafter, their kidneys were harvested for histopathology analysis, and their blood was collected for hematological analysis. In the H&E results (Figure 3b), Magnevist exacerbated the tissue damage in the kidneys and caused a higher degree of epithelial damage that extended to deeper portions of the renal cortex than was observed in the cisplatin- and nIBCA-treated groups. Approximately 80% of the tubules had evidence of epithelial loss manifested by an increase in luminal diameter and abundant cellular casts. Individual renal tubular cell necrosis in both the cisplatin- and Magnevist-treated groups was also more frequent than that in the nIBCA-treated groups. Histopathological changes in the nIBCA groups were comparable to the cisplatin group with regard to severity and distribution. Magnevist further deteriorated the GFR of the kidneys, which led to a surge in the creatine and BUN indexes. In contrast, nIBCA didn't further affect the GFR and kept the same level in the kidney panel index with the cisplatin-treated controls (Figure 3c and 3d). The administration Magnevist also caused some obvious side effects. For instance, the Magnevist-treated mice (with KD) lost hair and had a pronounced limp in their hind legs, while the nIBCA treated group didn't show any obvious difference in appearance and behaviors from the cisplatin control group. This evidence further supported the conclusion that nIBCA was much safer than Magnevist. By using this well-established KD model, we systemically investigated the nephrotoxicity of the nIBCA and Magnevist. These results indicate that nIBCA less toxic than Magnevist to the kidneys and are potentially an alternative to Magnevist in tumor T_1 MRI diagnosis, especially on the patients who are suffering from kidney disease.

3.6. Pharmacokinetics of nIBCA

The micellar nanostructure was supposed to confer the nano-enabled contrast agent (nIBCA) with better blood circulation than the small-molecule contrast agent (GBCA). Therefore, the

pharmacokinetics of Magnevist and nIBCA were evaluated. The results were shown in Figure 4. The nIBCA showed much better pharmacokinetic than Magnevist. The AUC of nIBCA was 52.2 times larger than that of Magnevist. The half-time of Magnevist was 14.7 min in the distribution phase ($T_{1/2}$ α) and 47.1 min in the elimination phase ($T_{1/2}$ β). In striking contrast, nIBCA showed 31.3 min of $T_{1/2}$ α and 2888 min of $T_{1/2}$ β, which are ~2 times and ~61 times longer than these of Magnevist, respectively. The better blood circulation may explain why the nIBCA exhibited longer effective imaging window.

3.7. Biodistributions of nIBCA

To further understand the biological actions of nIBCA, the biodistributions of nIBCA were evaluated. Iron concentrations were quantitatively analyzed by inductively coupled plasma mass spectrometry (ICP-MS), as shown in Figure S17, nIBCA showed low accumulations in heart, kidney and lung. The low kidney accumulation was consistent with the MRI results of the kidney imaging (Figure 2a, lower panel), which further confirmed that the nIBCA is potentially safe to patients with kidney disease. As expected, nIBCA was taken into the reticuloendothelial system (liver and spleen) in a similar fashion to most other nanoparticles. [62, 65, 66] Besides that, the nanoprobe showed an excellent accumulation in the tumor, which may explain why the nIBCA showed excellent MRI capabilities and a high TNR.

3.8. Imaging of intracranial brain tumor by using nIBCA as contrast agents.

Since the nIBCA exhibited high TNR and could more effectively differentiate between tumor and normal tissue, we sought to further evaluate nIBCA in an orthotopic model that is more clinically relevant than a subcutaneous model. Therefore, we evaluated the MRI capabilities of nIBCA to detect deeply embedded brain tumors. To establish the mouse model of an orthotopic brain tumor, U251 MG cells were directly inoculated into the brain of a mouse with a microliter syringe (Figure 5a). Then, the skin on the head was sutured. The mice were given analgesics to relieve the pain. The mice developed intracranial brain tumors in two weeks. nIBCA was administered by i.v. to the mice and could readily enhance the T_1 contrast in the tumor region in the mouse brain (Figure 5b). The T_1 signal from nIBCA showed a significantly stronger signal in the tumor site (Figure 5c), and the TNR was also significantly enhanced for 2 times (Figure 5d) when compared with the mouse before the nIBCA administration. To further confirm the accuracy of the nIBCA-mediated imaging, the mouse was sacrificed for histopathological analysis of brain tissue and the tumor region is marked by the dark red area (Figure 5e). The tumor pattern delineated by the nIBCA-enhanced MRI was quite similar to that in the histopathological analysis, indicating that the nIBCA was valuable for tumor diagnosis based on MRI.

3.9. Tumor selectivity of nIBCA

The tumor and normal tissue distributions of nIBCA determine the TNR of tumor MRI. Therefore, the intracranial tumor selectivity of nIBCA was investigated by fluorescence imaging. To make nIBCA traceable, hydrophobic dye (DiD) was encapsulated into nIBCA and formed a fluorescent nanoparticle (nIBCA@DiD). The nIBCA@DiD was i.v. administrated into mice with intracranial tumor. 24 h later, the whole brain of mice was harvest and cryo-sliced for CLSM observation. As shown in Figure 6a, nIBCA selectively accumulated in tumor site (the nuclei are denser as indicated by Hoechst 33342). In the

images of higher magnification, nIBCA@DiD can differentiate the boundary between the normal tissue and tumor. The tumor location in the brain was confirmed by H&E staining corresponded to that in CLSM image (Figure 6b, upper panel). The boundary between tumor and normal tissue was also differentiated by H&E staining and corelated well with that in CLSM image (Figure 6b, lower panel). The CLSM and H&E results demonstrated that nIBCA selectively accumulated in the tumor site, which may contribute to high TNR of nIBCA-mediated MRI.

3.10. Systemic toxicity of nIBCA

The systemic toxicity of nIBCA was investigated by histopathology and hematology. As shown in Figure 7a, the administration of nIBCA didn't cause any obvious alterations to the normal tissues, including the liver and spleen, in comparison with those from PBS-treated mice. In the hematology results, there was no significant difference between the nIBCA and PBS treated mice on the ALT and AST parameters, indicating that nIBCA didn't cause any hepatotoxicity. This lack of toxicity in the liver and other organs may also be ascribed to the low toxicity of iron. The other blood chemical indexes of the nIBCA treated mice were also evaluated, and none of them exhibited toxicity, comparing to the normal mice. By combing the results of hemolysis (Figure 1e), histopathology (Figure 7a) and hematology (Figure 7b), we confirmed that nIBCA was with high biocompatibility.

4. Conclusions

In this work, we developed a new nephrotoxicity-free, nano-enabled MRI CA by the coordination of iron into a micellar structure with a PEG surface. This CA selectively accumulated in tumor sites and significantly improved the TNR. In comparison with commercial GBCA (Magnevist), nIBCA induced less nephrotoxicity evidenced by H&E and the levels of creatine and BUN, which indicates that it could be an alternative MRI contrast agent for patients with kidney insufficiency. The nIBCA also highlighted both subcutaneous and intracranial brain tumors and clearly differentiated the margin between the tumor and normal tissue with high TNR. The effective imaging window of nIBCA can last for at least 24 h, which was 24-time longer than the conventional GBCA (Magnevist). This iron-based contrast agent is highly safe, showed excellent selectivity, and will potentially be the next generation MRI CAs for tumor diagnosis and an alternative option to GBCAs, especially for patients who are suffering from kidney disease.

Supplementary Material

Refer to Web version on PubMed Central for supplementary material.

Acknowledgments

References

[1]. Greene FL, Balch CM, Fleming ID, Fritz A, Haller DG, Morrow M, Page DL, AJCC cancer staging handbook: TNM classification of malignant tumors, Springer Science & Business Media, 2002.

[2]. Gambhir SS, Molecular imaging of cancer with positron emission tomography, Nat. Rev. Cancer 2(9) (2002) 683–693. [PubMed: 12209157]

[3]. Lardinois D, Weder W, Hany TF, Kamel EM, Korom S, Seifert B, von Schulthess GK, Steinert HC, Staging of Non–Small-Cell Lung Cancer with Integrated Positron-Emission Tomography and Computed Tomography, N. Engl. J. Med 348(25) (2003) 2500–2507. [PubMed: 12815135]

[4]. Edward Coleman R, Single photon emission computed tomography and positron emission tomography in cancer imaging, Cancer 67(S4) (1991) 1261–1270. [PubMed: 1991287]

[5]. Wiele C.V.d., Lahorte C, Vermeersch H, Loose D, Mervillie K, Steinmetz ND, Vanderheyden J-L, Cuvelier CA, Slegers G, Dierck RA, Quantitative Tumor Apoptosis Imaging Using Technetium-99m–HYNIC Annexin V Single Photon Emission Computed Tomography, J. Clin. Oncol 21(18) (2003) 3483–3487. [PubMed: 12972524]

[6]. Xue X, Zhao Y, Dai L, Zhang X, Hao X, Zhang C, Huo S, Liu J, Liu C, Kumar A, Chen W-Q, Zou G, Liang X-J, Spatiotemporal Drug Release Visualized through a Drug Delivery System with Tunable Aggregation-Induced Emission, Adv. Mater 26(5) (2014) 712–717. [PubMed: 24129910]

[7]. Xue X, Jin S, Zhang C, Yang K, Huo S, Chen F, Zou G, Liang X-J, Probe-Inspired Nano-Prodrug with Dual-Color Fluorogenic Property Reveals Spatiotemporal Drug Release in Living Cells, ACS Nano 9(3) (2015) 2729–2739. [PubMed: 25688453]

[8]. Xue X, Huang Y, Bo R, Jia B, Wu H, Yuan Y, Wang Z, Ma Z, Jing D, Xu X, Yu W, Lin T.-y., Li Y, Trojan Horse nanotheranostics with dual transformability and multifunctionality for highly effective cancer treatment, Nat. Commun 9(1) (2018) 3653. [PubMed: 30194413]

[9]. Na HB, Song IC, Hyeon T, Inorganic Nanoparticles for MRI Contrast Agents, Adv. Mater 21(21) (2009) 2133–2148.

[10]. Kobayashi H, Brechbiel MW, Nano-sized MRI contrast agents with dendrimer cores, Adv. Drug Deliver. Rev 57(15) (2005) 2271–2286.

[11]. Na HB, Lee JH, An K, Park YI, Park M, Lee IS, Nam D-H, Kim ST, Kim S-H, Kim S-W, Lim K-H, Kim K-S, Kim S-O, Hyeon T, Development of a T1 Contrast Agent for Magnetic Resonance Imaging Using MnO Nanoparticles, Angew. Chem. Int. Ed 46(28) (2007) 5397–5401.

[12]. Bulte JWM, Kraitchman DL, Iron oxide MR contrast agents for molecular and cellular imaging, NMR Biomed. 17(7) (2004) 484–499. [PubMed: 15526347]

[13]. Conijn MMA, Geerlings MI, Luijten PR, Zwanenburg JJM, Visser F, Biessels GJ, Hendrikse J, Visualization of cerebral microbleeds with dual-echo T2*-weighted magnetic resonance imaging at 7.0 T, J. Magn. Reson. Imaging 32(1) (2010) 52–59. [PubMed: 20578010]

[14]. Caravan P, Strategies for increasing the sensitivity of gadolinium based MRI contrast agents, Chem. Soc. Rev 35(6) (2006) 512–523. [PubMed: 16729145]

[15]. Ananta JS, Godin B, Sethi R, Moriggi L, Liu X, Serda RE, Krishnamurthy R, Muthupillai R, Bolskar RD, Helm L, Ferrari M, Wilson LJ, Decuzzi P, Geometrical confinement of gadolinium-based contrast agents in nanoporous particles enhances T1 contrast, Nat. Nanotechnol 5 (2010) 815. [PubMed: 20972435]

[16]. Cheng Z, Thorek DLJ, Tsourkas A, Gadolinium-Conjugated Dendrimer Nanoclusters as a Tumor-Targeted T1 Magnetic Resonance Imaging Contrast Agent, Angew. Chem. Int. Ed 49(2) (2010) 346–350.

[17]. Zhou Z, Lu Z-R, Gadolinium-based contrast agents for magnetic resonance cancer imaging, WIREs: Nanomed. Nanobiotech 5(1) (2013) 1–18.

[18]. Ersoy H, Rybicki FJ, Biochemical safety profiles of gadolinium-based extracellular contrast agents and nephrogenic systemic fibrosis, J. Magn. Resonan. Imaging 26(5) (2007) 1190–1197.

[19]. Kuo PH, Kanal E, Abu-Alfa AK, Cowper SE, Gadolinium-based MR Contrast Agents and Nephrogenic Systemic Fibrosis, Radiology 242(3) (2007) 647–649. [PubMed: 17213364]

[20]. Kanda T, Fukusato T, Matsuda M, Toyoda K, Oba H, J.i. Kotoku, Haruyama T, Kitajima K, Furui S, Gadolinium-based Contrast Agent Accumulates in the Brain Even in Subjects without Severe Renal Dysfunction: Evaluation of Autopsy Brain Specimens with Inductively Coupled Plasma Mass Spectroscopy, Radiology 276(1) (2015) 228–232. [PubMed: 25942417]

[21]. McDonald RJ, McDonald JS, Kallmes DF, Jentoft ME, Murray DL, Thielen KR, Williamson EE, Eckel LJ, Intracranial Gadolinium Deposition after Contrast-enhanced MR Imaging, Radiology 275(3) (2015) 772–782. [PubMed: 25742194]

[22]. Dekkers IA, Roos R, van der Molen AJ, Gadolinium retention after administration of contrast agents based on linear chelators and the recommendations of the European Medicines Agency, Eur. Radiol 28(4) (2018) 1579–1584. [PubMed: 29063255]

[23]. Yang L, Krefting I, Gorovets A, Marzella L, Kaiser J, Boucher R, Rieves D, Nephrogenic Systemic Fibrosis and Class Labeling of Gadolinium-based Contrast Agents by the Food and Drug Administration, Radiology 265(1) (2012) 248–253. [PubMed: 22923714]

[24]. Clough TJ, Jiang L, Wong K-L, Long NJ, Ligand design strategies to increase stability of gadolinium-based magnetic resonance imaging contrast agents, Nat. Commun 10(1) (2019) 1420. [PubMed: 30926784]

[25]. Pasquini L, Napolitano A, Visconti E, Longo D, Romano A, Tomà P, Espagnet MCRJCD, Gadolinium-Based Contrast Agent-Related Toxicities, CNS Drugs 32(3) (2018) 229–240. [PubMed: 29508245]

[26]. Olchowy C, Cebulski K, Łasecki M, Chaber R, Olchowy A, Kałwak K, Zaleska-Dorobisz U, The presence of the gadolinium-based contrast agent depositions in the brain and symptoms of gadolinium neurotoxicity - A systematic review, PLOS ONE 12(2) (2017) e0171704. [PubMed: 28187173]

[27]. Bae KH, Lee K, Kim C, Park TG, Surface functionalized hollow manganese oxide nanoparticles for cancer targeted siRNA delivery and magnetic resonance imaging, Biomaterials 32(1) (2011) 176–184. [PubMed: 20934746]

[28]. Shin J, Anisur RM, Ko MK, Im GH, Lee JH, Lee IS, Hollow Manganese Oxide Nanoparticles as Multifunctional Agents for Magnetic Resonance Imaging and Drug Delivery, Angew. Chem. Int. Ed 48(2) (2009) 321–324.

[29]. Kim T, Cho E-J, Chae Y, Kim M, Oh A, Jin J, Lee E-S, Baik H, Haam S, Suh J-S, Huh Y-M, Lee K, Urchin-Shaped Manganese Oxide Nanoparticles as pH-Responsive Activatable T1 Contrast Agents for Magnetic Resonance Imaging, Angew. Chem. Int. Ed 50(45) (2011) 10589–10593.

[30]. Zhao Z, Zhou Z, Bao J, Wang Z, Hu J, Chi X, Ni K, Wang R, Chen X, Chen Z, Gao J, Octapod iron oxide nanoparticles as high-performance T2 contrast agents for magnetic resonance imaging, Nat. Commun 4 (2013) 2266. [PubMed: 23903002]

[31]. Jang J.-t., Nah H, Lee J-H, Moon SH, Kim MG, Cheon J, Critical Enhancements of MRI Contrast and Hyperthermic Effects by Dopant-Controlled Magnetic Nanoparticles, Angew. Chem. Int. Ed 121(7) (2009) 1260–1264.

[32]. Lee N, Hyeon T, Designed synthesis of uniformly sized iron oxide nanoparticles for efficient magnetic resonance imaging contrast agents, Chem. Soc. Rev 41(7) (2012) 2575–2589. [PubMed: 22138852]

[33]. Lu Y, Xu Y-J, Zhang G.-b., Ling D, Wang M.-q., Zhou Y, Wu Y-D, Wu T, Hackett MJ, Hyo Kim B, Chang H, Kim J, Hu X-T, Dong L, Lee N, Li F, He J-C, Zhang L, Wen H-Q, Yang B, Hong Choi S, Hyeon T, Zou D-H, Iron oxide nanoclusters for T1 magnetic resonance imaging of non-human primates, Nat. Biomed. Eng 1(8) (2017) 637–643. [PubMed: 31015599]

[34]. Sandiford L, Phinikaridou A, Protti A, Meszaros LK, Cui X, Yan Y, Frodsham G, Williamson PA, Gaddum N, Botnar RM, Blower PJ, Green MA, de Rosales RTM, Bisphosphonate-Anchored PEGylation and Radiolabeling of Superparamagnetic Iron Oxide: Long-Circulating Nanoparticles for in Vivo Multimodal (T1 MRI-SPECT) Imaging, ACS Nano 7(1) (2013) 500–512. [PubMed: 23194247]

[35]. Kim BH, Lee N, Kim H, An K, Park YI, Choi Y, Shin K, Lee Y, Kwon SG, Na HB, Park J-G, Ahn T-Y, Kim Y-W, Moon WK, Choi SH, Hyeon T, Large-Scale Synthesis of Uniform and Extremely Small-Sized Iron Oxide Nanoparticles for High-Resolution T1 Magnetic Resonance Imaging Contrast Agents, J. Am. Chem. Soc 133(32) (2011) 12624–12631. [PubMed: 21744804]

[36]. Chen H, Zhang W, Zhu G, Xie J, Chen X, Rethinking cancer nanotheranostics, Nat. Rev. Mater 2(7) (2017) 17024. [PubMed: 29075517]

[37]. Schwert DD, Richardson N, Ji G, Radüchel B, Ebert W, Heffner PE, Keck R, Davies JA, Synthesis of Two 3,5-Disubstituted Sulfonamide Catechol Ligands and Evaluation of Their Iron(III) Complexes for Use as MRI Contrast Agents, J. Med. Chem 48(23) (2005) 7482–7485. [PubMed: 16279808]

[38]. Miao Y, Xie F, Cen J, Zhou F, Tao X, Luo J, Han G, Kong X, Yang X, Sun J, Ling J, Fe3+@polyDOPA-b-polysarcosine, a T1-Weighted MRI Contrast Agent via Controlled NTA Polymerization, ACS Macro Lett. 7(6) (2018) 693–698.

[39]. Li Y, Huang Y, Wang Z, Carniato F, Xie Y, Patterson JP, Thompson MP, Andolina CM, Ditri TB, Millstone JE, Figueroa JS, Rinehart JD, Scadeng M, Botta M, Gianneschi NC, Polycatechol Nanoparticle MRI Contrast Agents, Small 12(5) (2016) 668–677. [PubMed: 26681255]

[40]. Saowalak K, Titipun T, Somchai T, Chalermchai P, Iron(III)-Tannic Molecular Nanoparticles Enhance Autophagy effect and T1 MRI Contrast in Liver Cell Lines, Sci. Rep 8(1) (2018) 6647. [PubMed: 29703912]

[41]. Wang Z, Xue X, Lu H, He Y, Lu Z, Chen Z, Yuan Y, Tang N, Dreyer CA, Quigley L, Curro N, Lam KS, Walton JH, Lin T.-y., Louie AY, Gilbert DA, Liu K, Ferrara KW, Li Y, Two-way magnetic resonance tuning and enhanced subtraction imaging for non-invasive and quantitative biological imaging, Nat. Nanotechnol 15(6) (2020) 482–490. [PubMed: 32451501]

[42]. Fang J, Nakamura H, Maeda H, The EPR effect: Unique features of tumor blood vessels for drug delivery, factors involved, and limitations and augmentation of the effect, Adv. Drug Deliv. Rev 63(3) (2011) 136–151. [PubMed: 20441782]

[43]. Maeda H, Wu J, Sawa T, Matsumura Y, Hori K, Tumor vascular permeability and the EPR effect in macromolecular therapeutics: a review, J. Control. Release 65(1–2) (2000) 271–284. [PubMed: 10699287]

[44]. Xue X, Huang Y, Wang X, Wang Z, Carney RP, Li X, Yuan Y, He Y, Lin T.-y., Li Y, Self-indicating, fully active pharmaceutical ingredients nanoparticles (FAPIN) for multimodal imaging guided trimodality cancer therapy, Biomaterials 161 (2018) 203–215. [PubMed: 29421556]

[45]. Sindhwani S, Syed AM, Ngai J, Kingston BR, Maiorino L, Rothschild J, MacMillan P, Zhang Y, Rajesh NU, Hoang T, Wu JLY, Wilhelm S, Zilman A, Gadde S, Sulaiman A, Ouyang B, Lin Z, Wang L, Egeblad M, Chan WCW, The entry of nanoparticles into solid tumours, Nat. Mater 19(5) (2020) 566–575. [PubMed: 31932672]

[46]. Liu J, Yu M, Zhou C, Yang S, Ning X, Zheng J, Passive Tumor Targeting of Renal-Clearable Luminescent Gold Nanoparticles: Long Tumor Retention and Fast Normal Tissue Clearance, J. Am. Chem. Soc 135(13) (2013) 4978–4981. [PubMed: 23506476]

[47]. Yang X, Xue X, Luo Y, Lin T.-y., Zhang H, Lac D, Xiao K, He Y, Jia B, Lam KS, Li Y, Sub-100nm, long tumor retention SN-38-loaded photonic micelles for tri-modal cancer therapy, J. Control. Release 261 (2017) 297–306. [PubMed: 28700898]

[48]. Bartlett DW, Su H, Hildebrandt IJ, Weber WA, Davis ME, Impact of tumor-specific targeting on the biodistribution and efficacy of siRNA nanoparticles measured by multimodality in vivo imaging, Proc. Natl. Acad. Sci. U. S. A 104(39) (2007) 15549–15554. [PubMed: 17875985]

[49]. Rabin O, Manuel Perez J, Grimm J, Wojtkiewicz G, Weissleder R, An X-ray computed tomography imaging agent based on long-circulating bismuth sulphide nanoparticles, Nat. Mater 5(2) (2006) 118–122. [PubMed: 16444262]

[50]. Li Y, Xiao W, Xiao K, Berti L, Luo J, Tseng HP, Fung G, Lam KS, Well-Defined, Reversible Boronate Crosslinked Nanocarriers for Targeted Drug Delivery in Response to Acidic pH Values and cis-Diols, Angew. Chem. Int. Ed 51(12) (2012) 2864–2869.

[51]. Lin TY, Li Y, Liu Q, Chen JL, Zhang H, Lac D, Zhang H, Ferrara KW, Wachsmann-Hogiu S, Li T, Airhart S, deVere White R, Lam KS, Pan CX, Novel theranostic nanoporphyrins for photodynamic diagnosis and trimodal therapy for bladder cancer, Biomaterials 104 (2016) 339–51. [PubMed: 27479049]

[52]. Li Y, Lin T.-y., Luo Y, Liu Q, Xiao W, Guo W, Lac D, Zhang H, Feng C, Wachsmann-Hogiu S, Walton JH, Cherry SR, Rowland DJ, Kukis D, Pan C, Lam KS, A smart and versatile theranostic

nanomedicine platform based on nanoporphyrin, Nat. Commun 5 (2014) 4712. [PubMed: 25158161]

[53]. Qin W, Ding D, Liu J, Yuan WZ, Hu Y, Liu B, Tang BZ, Biocompatible Nanoparticles with Aggregation-Induced Emission Characteristics as Far-Red/Near-Infrared Fluorescent Bioprobes for In Vitro and In Vivo Imaging Applications, Adv. Funct. Mater 22(4) (2012) 771–779.

[54]. Wang S, Liu J, Feng G, Ng LG, Liu B, NIR-II Excitable Conjugated Polymer Dots with Bright NIR-I Emission for Deep In Vivo Two-Photon Brain Imaging Through Intact Skull, Adv. Funct. Mater 29(15) (2019) 1808365.

[55]. Lin G, Manghnani PN, Mao D, Teh C, Li Y, Zhao Z, Liu B, Tang BZ, Robust Red Organic Nanoparticles for In Vivo Fluorescence Imaging of Cancer Cell Progression in Xenografted Zebrafish, Adv. Funct. Mater 27(31) (2017) 1701418.

[56]. Mohr A, Talbiersky P, Korth H-G, Sustmann R, Boese R, Bläser D, Rehage H, A New Pyrene-Based Fluorescent Probe for the Determination of Critical Micelle Concentrations, J. Phys. Chem. B 111(45) (2007) 12985–12992. [PubMed: 17958349]

[57]. Aguiar J, Carpena P, Molina-Bolívar JA, Carnero Ruiz C, On the determination of the critical micelle concentration by the pyrene 1:3 ratio method, J. Colloid Interface Sci 258(1) (2003) 116–122.

[58]. Sedó J, Saiz-Poseu J, Busqué F, Ruiz-Molina D, Catechol-Based Biomimetic Functional Materials, Adv. Mater 25(5) (2013) 653–701. [PubMed: 23180685]

[59]. Azevedo S, Costa AMS, Andersen A, Choi IS, Birkedal H, Mano JF, Bioinspired Ultratough Hydrogel with Fast Recovery, Self-Healing, Injectability and Cytocompatibility, Adv. Mater 29(28) (2017) 1700759.

[60]. Kawabata T, Schepkin V, Haramaki N, Phadke RS, Packer L, Iron coordination by catechol derivative antioxidants, Biochem. Pharm 51(11) (1996) 1569–1577. [PubMed: 8630099]

[61]. Owens DE, Peppas NA, Opsonization, biodistribution, and pharmacokinetics of polymeric nanoparticles, Int. J. Pharm 307(1) (2006) 93–102. [PubMed: 16303268]

[62]. Moghimi SM, Szebeni J, Stealth liposomes and long circulating nanoparticles: critical issues in pharmacokinetics, opsonization and protein-binding properties, Prog. Lipid Res 42(6) (2003) 463–478. [PubMed: 14559067]

[63]. Rabe M, Schaefer F, Non-Transgenic Mouse Models of Kidney Disease, Nephron 133(1) (2016) 53–61. [PubMed: 27212380]

[64]. Torres R, Velazquez H, Chang JJ, Levene MJ, Moeckel G, Desir GV, Safirstein R, Three-Dimensional Morphology by Multiphoton Microscopy with Clearing in a Model of Cisplatin-Induced CKD, J. Am. Soc. Nephrol 27(4) (2016) 1102–1112. [PubMed: 26303068]

[65]. Hirn S, Semmler-Behnke M, Schleh C, Wenk A, Lipka J, Schäffler M, Takenaka S, Möller W, Schmid G, Simon U, Kreyling WG, Particle size-dependent and surface charge-dependent biodistribution of gold nanoparticles after intravenous administration, Eur. J. Pharm. Biopharm 77(3) (2011) 407–416. [PubMed: 21195759]

[66]. Li S-D, Huang L, Stealth nanoparticles: High density but sheddable PEG is a key for tumor targeting, J. Control. Release 145(3) (2010) 178–181. [PubMed: 20338200]
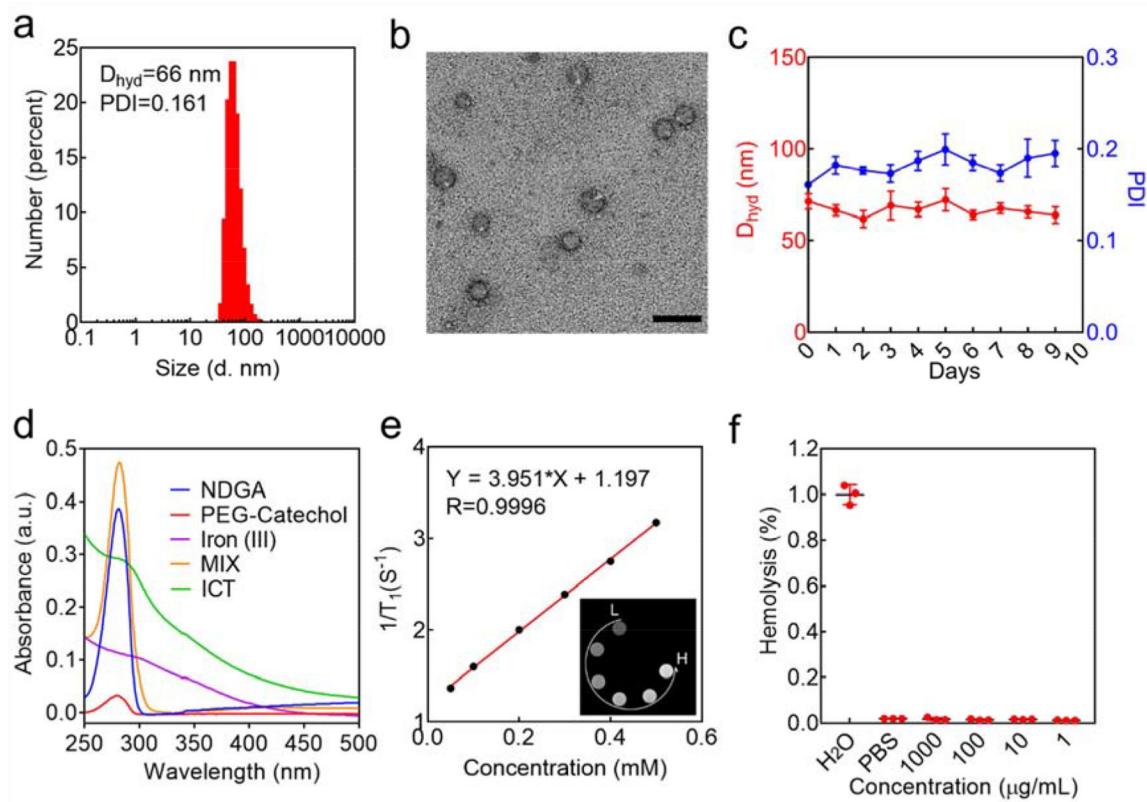
Figure 1. Characterization of the nIBCA.

a) Size distributions of nIBCA. The hydrodynamic diameter (D_{hyd}) and polydispersity index (PDI) were measured by dynamic light scattering (DLS). b) TEM showed the morphology of the nIBCA. The scale bar is 100 nm. c) Stability of nIBCA in the presence of 10% of fetal bovine serum. The size distribution and PDI were employed for stability evaluation. 0 day denote the fresh-made nIBCA. d) UV-vis spectra of PEG-catechol, NDGA, $FeCl_3$, physical mixture of the reactants (PEG-catechol, NDGA and $FeCl_3$) and ICT. The concentration of ICT was set as 5 μM. The reactants were set to their corresponding concentrations in ICT. e) Relaxivity (r_1) of nIBCA. The inset showed the MRI images. L, low concentration; H, high concentration. f) Hemolysis of nIBCA at different concentrations with water and PBS as a positive and negative control, respectively.
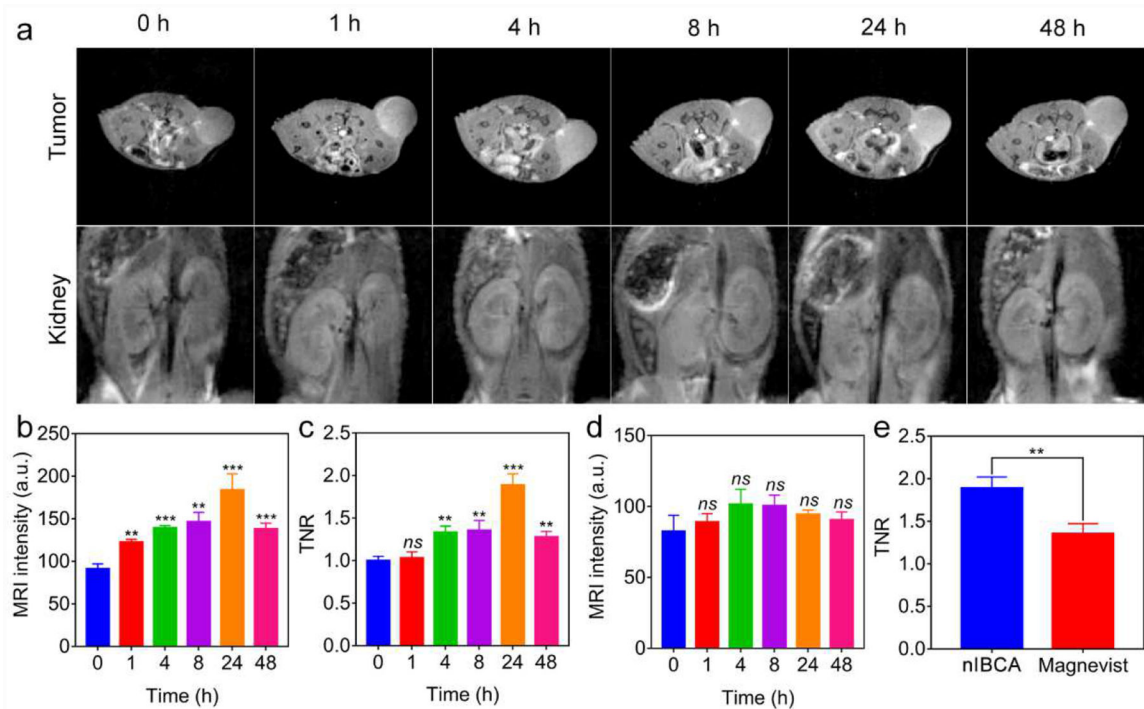
Figure 2. nIBCA-mediated T$_1$-weighted MRI in brain tumor (U251 MG) bearing mouse.
a) T$_1$-weighted MR images of the subcutaneous brain tumors (upper panel) and kidneys (lower panel) in nude mouse obtained at different timepoints after i.v. injection of nIBCA. 0 h indicates the timepoint before the administration of the contrast agent. b) Quantitative analysis of the MRI signal in the tumor. c) Tumor to normal tissue ratio (TNR) of the MRI signal on the mouse. d) Quantitative analysis of the MRI signal on the kidney. e) Comparison of TNR between nIBCA (24 h) and Magnevist (10 min) from the tumor MRI. Since the tumor accumulation time between nIBCA and Magnevist are different, the timepoints that showed the highest MRI signal were compared. The statistical analysis of b), c) and d) were compared with 0 h. *, p<0.05; **, p<0.01; ***, p<0.001; ns, not significantly. 100 mg/kg of nIBCA or 67 mg/kg of Magnevist were i.v. administrated into brain tumor-bearing mice (n=3). 100 mg/kg nIBCA and 67 mg/kg Magnevist contained the same amounts of the metal (iron in nIBCA and Gd in Magnevist).
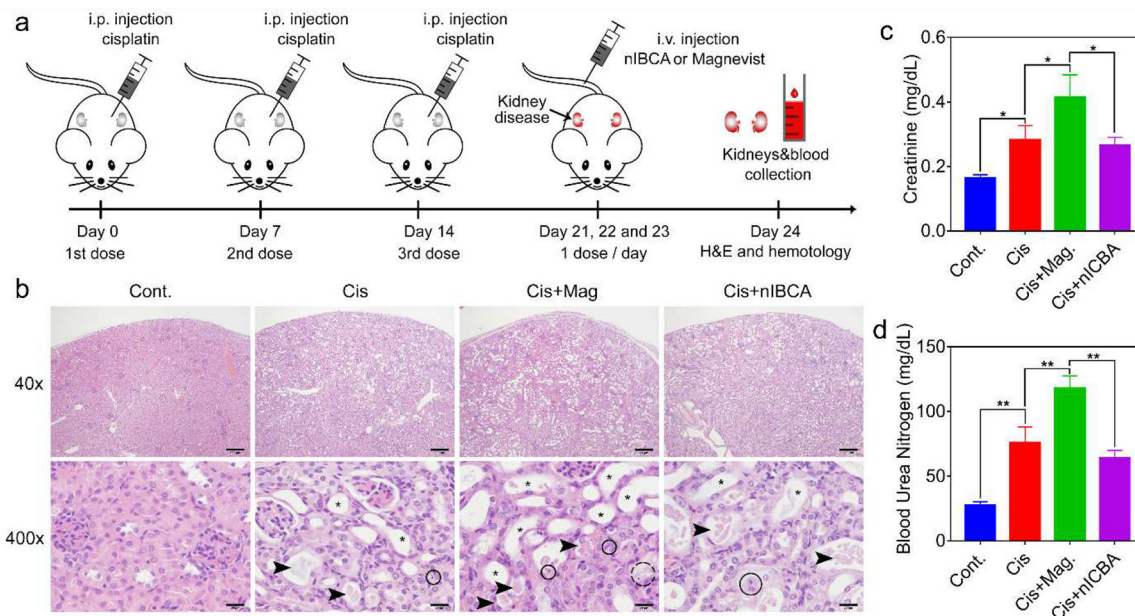
Figure 3. Nephrotoxicity of nIBCA and Magnevist on a mouse model of kidney disease.
a) The procedures for the establishment of the mouse model of KD and the following treatments. b) H&E analysis of the kidneys from the mice with different treatments. The results were presented at 40× and 400× magnification. Cont.: control mice without any treatment. Cis: mice treated with cisplatin to induce kidney disease. Cis+Mag: the mice with kidney disease treated with Magnevist. Cis+nIBCA, the mice with kidney disease treated with nIBCA. The white spaces represent increased luminal diameters of the proximal convoluted tubules due to epithelial loss and sloughing (asterisk). Cellular casts formed by the sloughed epithelial cells occlude the luminal space (arrow). Ballooning degeneration and individual cell necrosis are highlighted by dashed and solid circles, respectively. The scale bar in 40× is 200 μm, and 400× is 20 μm. c) Creatine and d) blood urea nitrogen (BUN) indexes of the mice (n=3). *, p<0.05; **, p<0.01. 100 mg/kg of nIBCA or 67 mg/kg of Magnevist were i.v. administrated into brain tumor-bearing mice (n=3). 100 mg/kg nIBCA and 67 mg/kg Magnevist contained the same amounts of the metal (iron in nIBCA and Gd in Magnevist).
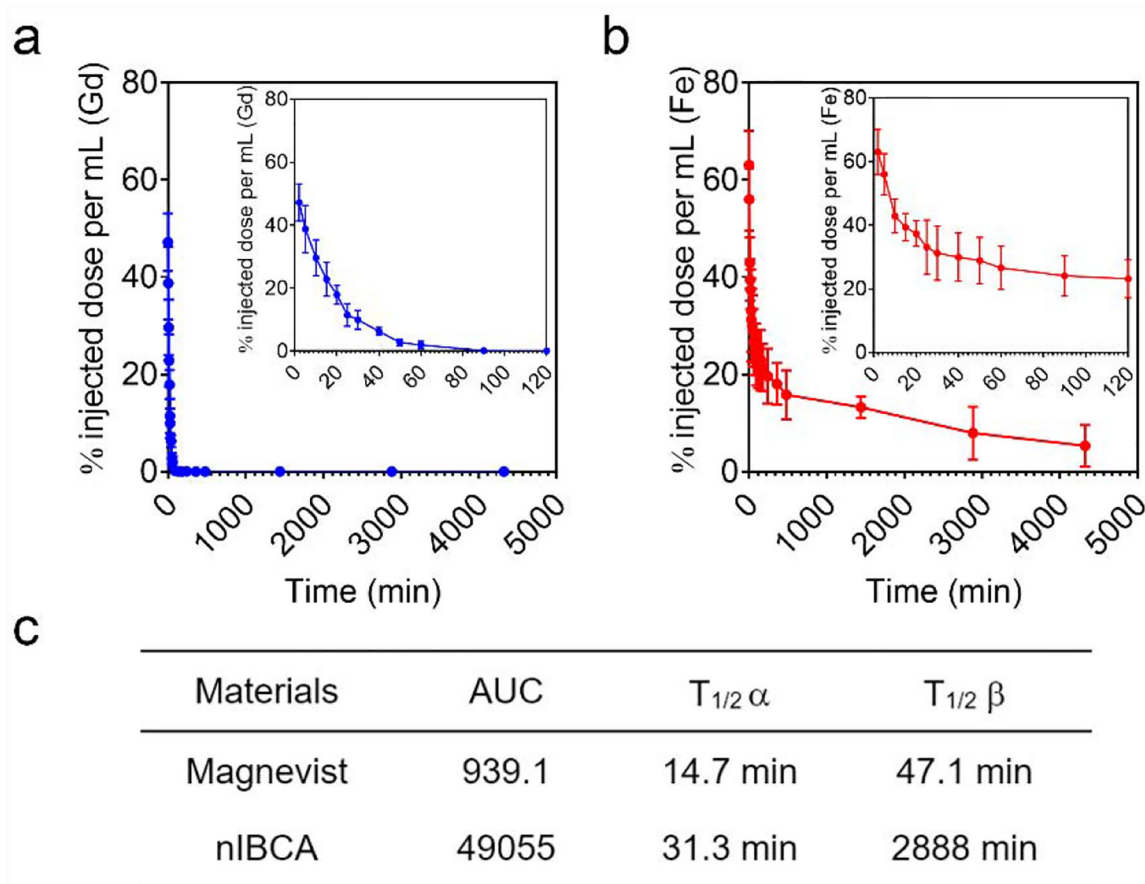
Figure 4. Pharmacokinetics (PK) of nIBCA.
PK profile of a) Magnevist and b) nIBCA in nude mice (n=3). The insets showed the PK profile from 0 to 120 min, due to the short circulation time of Magnevist. c) Quantification of PKs of Magnevist and nIBCA. AUC, area under the curve; $T_{1/2}$ α, distribution phase of circulation half-time; $T_{1/2}$ β, elimination phase.
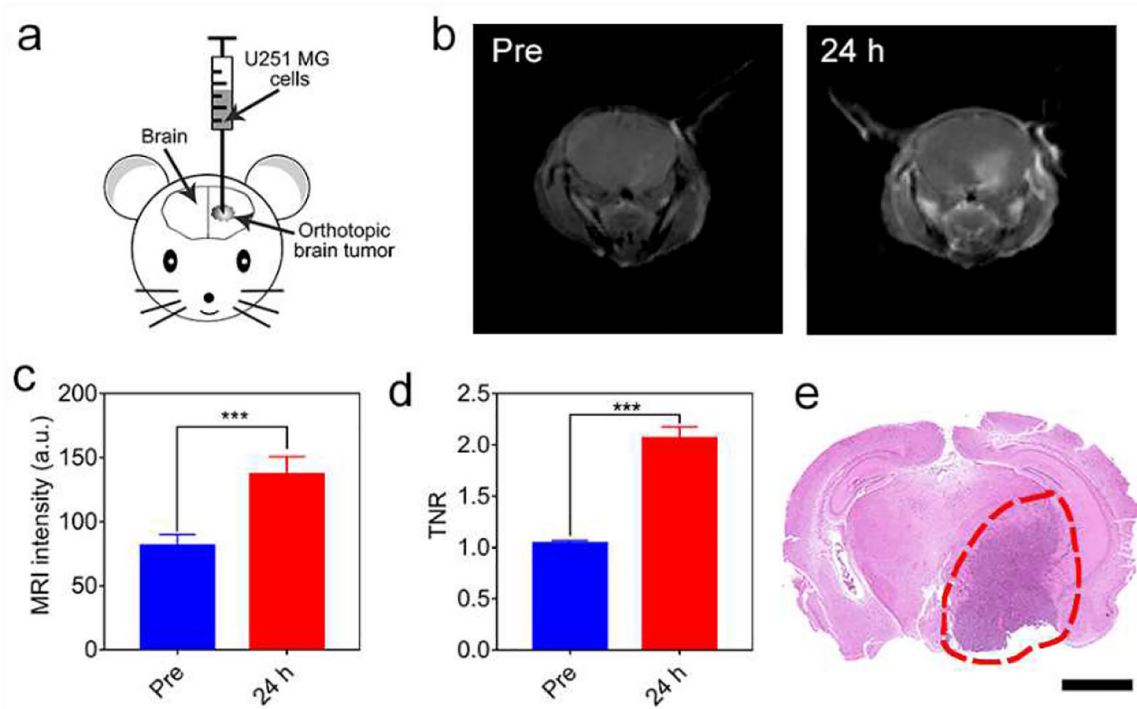
Figure 5. Application of nIBCA in intracranial brain tumor (U251 MG) diagnosis.
a) Schematic illustration of the establishment of the orthotopic brain tumor model. b) T_1-weighted MR images of orthotopic brain tumor by using nIBCA as a contrast agent. c) Quantitative analysis of the T_1 MRI signal of an orthotopic brain tumor. d) TNR of the T_1-weighted MRI in mouse brain tumor imaging. e) H&E staining that indicates the morphology, location, and size of the intracranial brain tumor. Red circle encloses the tumor tissue. The scale bar is 2 mm. ***, p<0.001. 100 mg/kg of nIBCA or 67 mg/kg of Magnevist were i.v. administrated into brain tumor-bearing mice (n=3). 100 mg/kg nIBCA and 67 mg/kg Magnevist contained the same amounts of the metal (iron in nIBCA and Gd in Magnevist).
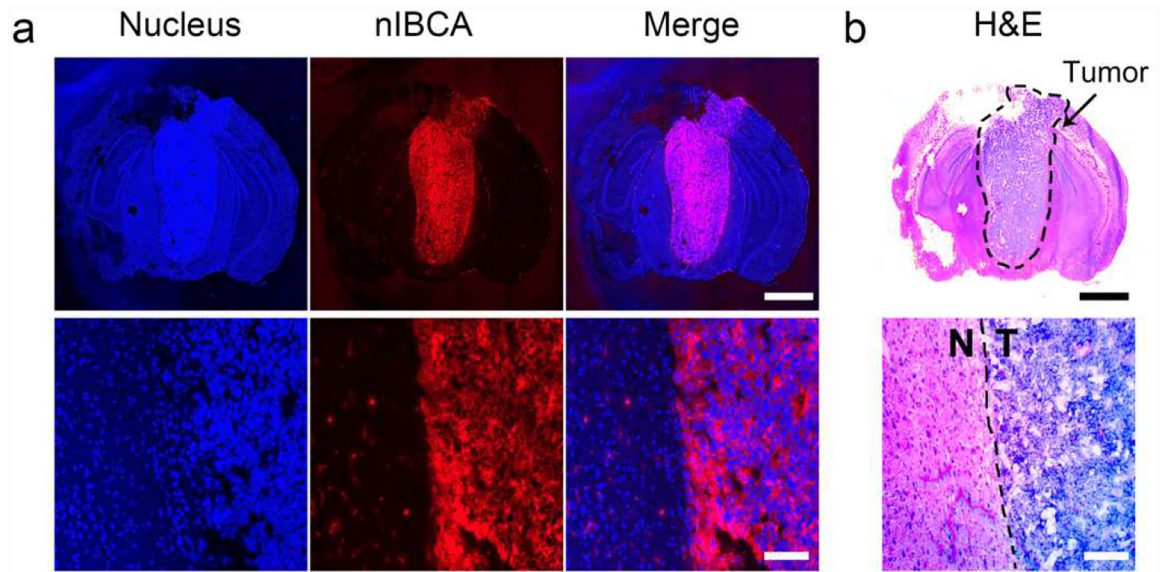
Figure 6. Tumor selectivity of nIBCA on an intracranial brain tumor.

a) CLSM images of nIBCA distribution in intracranial brain tumor. Upper panel, CLSM images of the whole brain, the scale bar is 2 mm. Lower panel, detailed tissue distribution of nIBCA by CLSM with high magnification, the scale bar is 100 μm. The whole-brain of mice was collected for cryo-section. The nuclei were stained with Hoechst 33342. The distribution of nIBCA was indicated by the fluorescence of DiD. B) H&E stain of the brain tissue. Upper panel, H&E image of the whole brain. The H&E slice was next to the one for CLSM and well-corresponded to the whole brain image of CLSM. The tumor tissue was enclosed in the black dash circle. The scale bar is 2 mm. Lower panel, the tumor/normal tissue boundary was differentiated at high magnification of optical microscope (not corresponding to CLSM image). The black dash line showed the boundary of the normal tissue and tumor tissue. N denotes normal tissue; T denotes tumor. The scale bar is 100 μm. The adjacent slice to the one for CLSM image was processed for H&E stain.
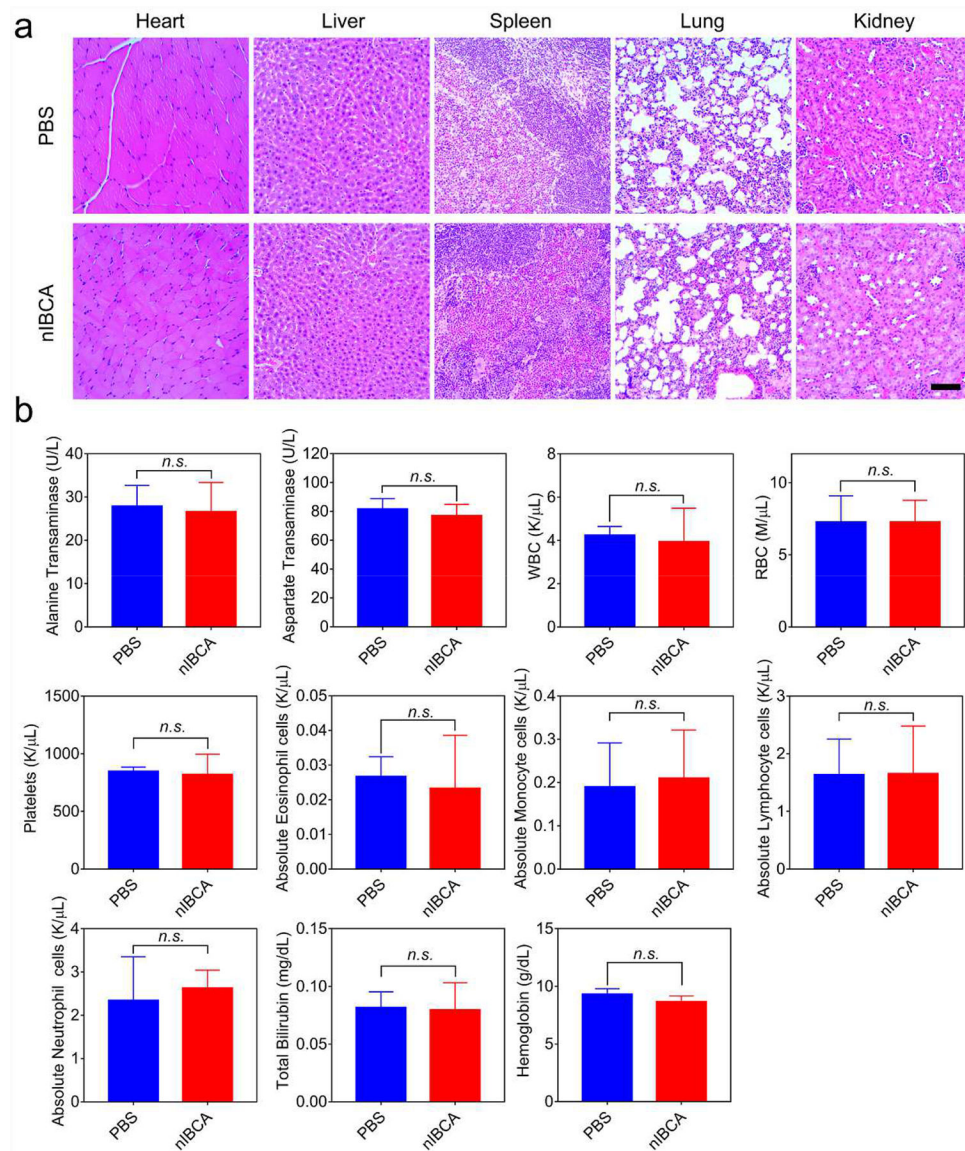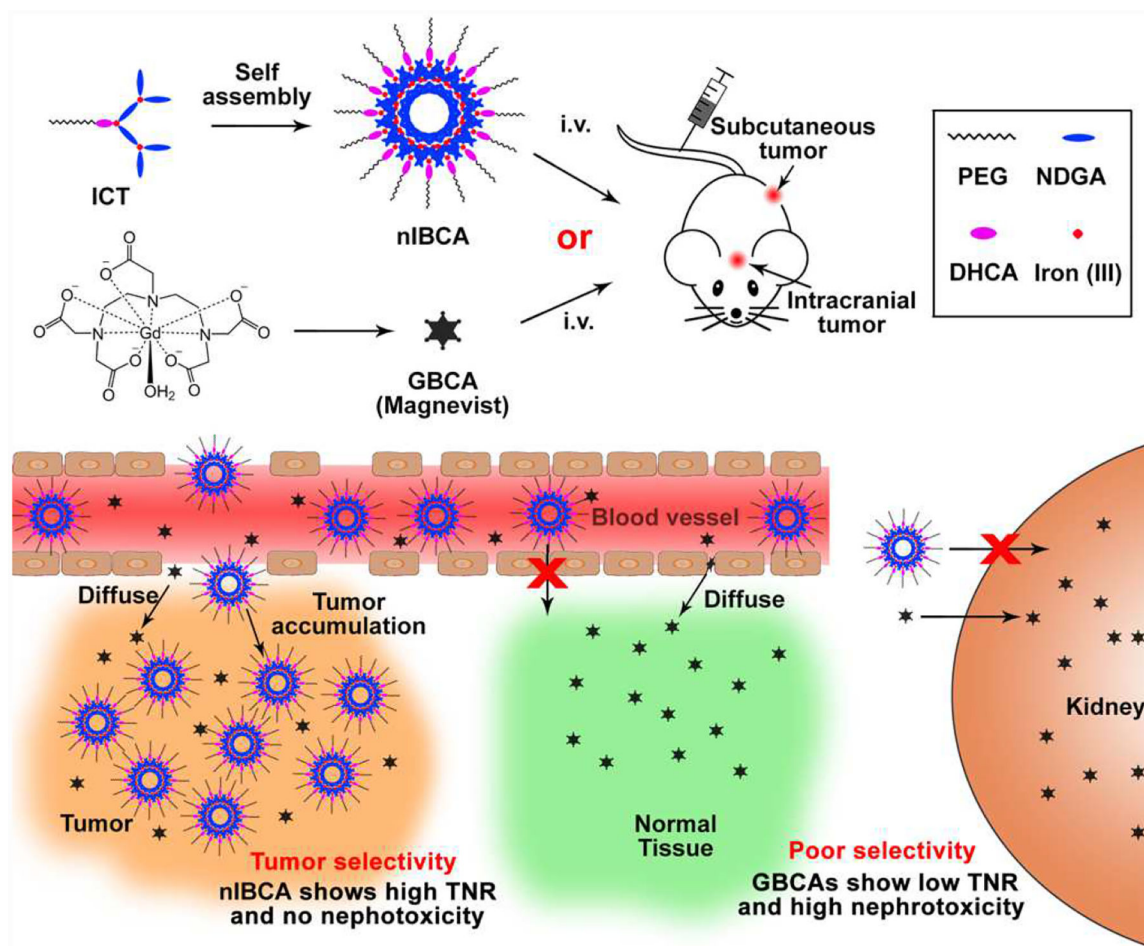
Figure 7. Systemic toxicity of nIBCA.

a) H&E stain of the main organs of the nIBCA treated mice. The scale bar is 100 μm. b) Hematology of nIBCA treated mice. The PBS-treated mice were employed as the normal controls.

Scheme 1. Schematic illustration of the advantages of nIBCA over a commercial GBCA.
The nIBCA selectively accumulates at the tumor site and had a significantly lower concentration in normal tissue. This selective accumulation enhances the MRI signal in the tumor site and has a high TNR. The GBCA not only infuses into tumor site, but also diffuses into normal tissues which result in a low TNR. GBCA is excreted through renal clearance and lead to a high accumulation of GBCA in the kidneys, which may be the main cause of NSF to patients with kidney disease. The nIBCA would not get to the kidneys and should, therefore, have little or no nephrotoxicity. Acronyms or abbreviations: ICT, iron-coordinated telodendrimer; PEG, polyethylene glycol; NDGA, nordihydroguaiaretic acid; DHCA, 3,4-dihydroxyhydrocinnamic acid; TNR, tumor to normal tissue ratio.